Measurement 259 (2026) 119559

Contents lists available at ScienceDirect

Measurement

journal homepage: www.elsevier.com/locate/measurement

# Measurement-based analysis of packaged X-Hall current sensors for automotive applications

Mattia Mengozzi [a,b,*], Sana Fatima Syeda [a,b], Jacopo Ferretti [a,c], Gian Piero Gibiino [a,b], Marco Crescentini [a,b], Pier Andrea Traverso [a]

[a] Department of Electrical, Electronic, and Information Engineering (DEI), University of Bologna, Italy
[b] Advanced Research Center on Electronic Systems (ARCES), University of Bologna, Italy
[c] High Performance Engineering s.r.l., Modena, Italy

ARTICLE INFO

*Keywords:*
Current sensing
Hall-effect sensors
Overcurrent protection
Measurement bench
Traction inverter
Dynamic characterization

ABSTRACT

This work presents a comprehensive experimental evaluation of X-Hall broadband current sensors, addressing system-level performance and measurement challenges relevant to modern power electronics. Two sensor versions (CH09 and CH10), fabricated using STMicroelectronics BCD10 process and packaged in ceramic (CLCC) and plastic (QFN) carriers, are analyzed in both high- and low-gain modes. The study examines the influence of process variation, packaging, and temperature on the static behavior of the sensors, while dynamic performance is characterized through small-signal frequency sweeps and large-signal step responses under both internal current and external magnetic field excitations. The most promising configuration—CH10 in the QFN package operating in low-gain mode—achieves an input-referred noise of 0.17 mT, a 1-dB compression range of 172 mT (60 dB dynamic range), with sensitivity and offset temperature dependencies of 0.61%/K and 0.11%/K, respectively. This configuration is further validated through preliminary integration into a silicon carbide (SiC) traction inverter and comparison with commercial alternatives.

## 1. Introduction

Current sensors play a crucial role in power electronics. They are used in a variety of applications such as feedback control loops in power converters [1] or fault detection and diagnosis (FDD) in power modules and motors [2]. All these applications, including those based on Artificial Intelligence (AI) [3,4], rely on the analysis of the current signal in the time domain, frequency domain, or a combination of both. As a general requirement, the current sensor must be compact and robust enough to be installed in power converters, while also offering a dynamic range on the order of hundreds of amperes [5]. Moreover, the bandwidth (BW) must span a broad spectrum, ranging from DC–kHz [6–9] for FDD applications to the MHz range for power module control and overcurrent protection [1,10].

Many typical current sensing technologies have fundamental limitations that hinder their adoption in this context. Shunt resistors, for example, can be permanently damaged by overcurrent and exhibit high power losses. Current transformers (CTs), on the other hand, cannot measure DC, and their core material is susceptible to saturation caused by high DC offsets. Furthermore, using a high winding ratio to measure near-DC frequency components reduces the measurement BW. The Rogowski coil (RC) suffers from the same issue when measuring near-DC components, and even fluxgate sensors exhibit BW limitations due to their windings [1,11].

While the typical BW reported for commercial devices [11] based on purely Hall-effect on-chip sensors is on the order of hundreds of kHz (with only a few recent products exceeding 1 MHz [12]), recent research activities have proposed novel devices and architectures that achieve acquisition BWs up to tens of MHz [13–16], demonstrating the viability of Hall sensors as a solution for fast-switching power electronic applications. Nevertheless, the literature mainly focuses on architectural solutions at the circuit level, without a detailed evaluation of system-level effects and characterization challenges, such as those arising from packaging and process-related issues that impact field application.

This work presents a comprehensive, measurement-based analysis of the non-ideal effects typical of broadband Hall-effect-based current sensors targeting power electronics for automotive applications, covering aspects ranging from chip-level non-idealities to measurement challenges and system integration effects. Specifically, this paper focuses on the characterization of two state-of-the-art, purely-Hall sensors based

* Corresponding author.
*E-mail address:* mattia.mengozzi3@unibo.it (M. Mengozzi).

https://doi.org/10.1016/j.measurement.2025.119559
Received 10 August 2025; Received in revised form 14 October 2025; Accepted 29 October 2025
Available online 6 November 2025

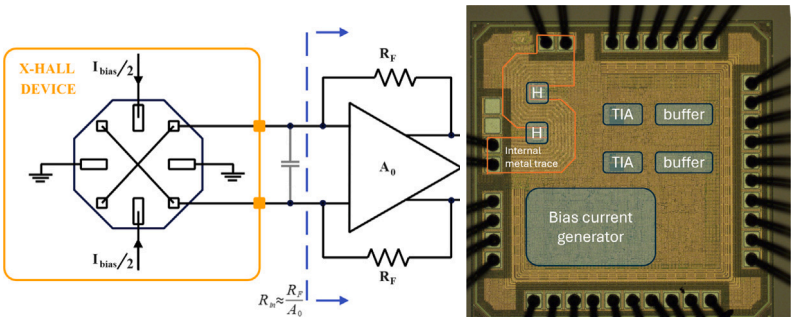


(a) (b)

**Fig. 1.** (a) General architecture of the X-Hall probe with current-mode readout using a resistive TIA. $I_{BIAS}$ is the Hall bias current, while $R_F$, $A_0$, and $R_{in}$ represent the feedback resistor, the differential amplifier gain, and the input resistance of the TIA, respectively. (b) Picture of the X-Hall silicon die incorporating two current sensors. The Hall probes are placed beneath the internal microstrip trace.

on the X-Hall architecture [15], which is designed to achieve MHz-range BWs by avoiding the so-called discrete-time spinning-current technique [17], traditionally employed to reduce offset effects at the sensor output.

The sensors under test are developed using the STMicroelectronics BCD process and are manufactured in two different packages, addressing a prototype for phase current monitoring and overcurrent protection in a Silicon Carbide (SiC)-based traction inverter. The SiC traction inverter developed for this case study is provided by High Performance Engineering s.r.l. (HPE), and is rated for 800 V and 250 kW, with a maximum phase current of 300 A.

The paper is organized as follows. Section 2 describes the sensor architecture and the available package carriers. In Section 3, the devices are tested by applying either a static current to the internal microstrip trace or an external static magnetic field. The findings are compared across the two considered carriers and the two implementations of the same topology, named CH09 and CH10. Section 4 analyzes the noise level and overall dynamic range of the sensors, while Section 5 focuses on temperature dependence. The dynamic behavior of the sensors is presented in Section 6, showing the response to both small-signal continuous wave (CW) currents as well as to large-signal steps either from current through the internal microstrip trace or from an external magnetic field. In Section 7, one sensor configuration is selected for preliminary validation when integrated with the HPE SiC inverter. Conclusions and future work are summarized in Section 8.

## 2. Description of the sensors

### 2.1. X-Hall architecture

The X-Hall topology for a purely-Hall effect-based integrated sensor was first proposed in [18] to overcome the BW limitations associated with the traditional spinning-current technique [17]. The X-Hall device consists of an 8-contact Hall-effect magnetic sensor (Fig. 1). However, due to its specific operating mode [15], it can be treated as a 4-contact Hall probe in which the bias and sensing contacts are fixed and cannot be exchanged. Unlike topologies based on the spinning technique, the X-Hall probe intrinsically implements a *static* offset cancellation method and can be operated in continuous-time mode (i.e., without the use of switches), thereby enhancing its BW capabilities. As a drawback, it features suboptimal performance in terms of residual offset [19,20].

To better exploit the BW capabilities of the X-Hall probe, a current-mode readout technique is implemented as proposed in [16] (shown on the right side in Fig. 1a). The current-mode readout nulls the Hall voltage generated by the X-Hall device using a transimpedance amplifier (TIA) and measures the current flowing out of the probe. This readout strategy overcomes the BW limitation imposed by the probe's parasitic capacitance by lowering the impedance at the node and the associated time constant, with the potential to achieve BWs greater than 10 MHz [16].

### 2.2. Sensor devices

Two different implementations of the X-Hall sensor with current-mode readout, referred to as CH09 and CH10, are experimentally evaluated. The CH09 implementation was detailed in [16], while the CH10 is an upgraded version of the CH09. Specifically, while both versions share the same sensing approach, the feedback resistor $R_F$ used in the TIA (Fig. 1) of CH10 is a p-doped unsilicided polysilicon resistor, which features lower process dispersion and a lower temperature coefficient. In contrast, CH09 uses an n-doped unsilicided polysilicon resistor, designed for high ohmic values. Moreover, the operational amplifier used in the TIA of CH10 employs larger transistors optimized for improved noise performance.

In addition, CH10 has the capability to bias the X-Hall probe at higher currents and integrates two measurement channels that can be combined for enhanced performance. However, to ensure a fair comparison, both implementations are analyzed here using a single measurement channel and the same bias current of 1 mA [16]. For both CH09 and CH10, the top thick metal layer hosts an S-shaped microstrip trace intended for low-current applications or testing purposes. This shape is designed to better focus the magnetic field generated by the current onto the Hall probe so as to maximize the device's sensitivity.

Packaging is a fundamental aspect of the system-level deployment of X-Hall sensors, as it enables the positioning of the sensor chip on a printed circuit board (PCB) and ensures electrical connectivity, environmental protection, and effective thermal management. The choice of packaging technology is critical, as it typically has a significant impact on overall performance.

In this study, both the CH09 and CH10 versions of the X-Hall sensor were assembled in two package types: a ceramic leadless chip carrier (CLCC) and a plastic quad-flat no-lead (QFN). The CLCC is a standard ceramic package and a preferred choice for power electronics prototypes, offering high thermal conductivity and electrical insulation.

The QFN package, by contrast, is used as a reference for plastic-based solutions and was selected in this case because it is one of the smallest available, allowing for lower parasitics. In addition, its low profile enables a reduced air gap in designs involving integration with a field concentrator, generally leading to higher magnetic field concentration and improved sensitivity. On the other hand, the QFN provides lower thermal and electrical isolation and is therefore less suitable for applications involving high currents through the internal microstrip.

In both cases, the silicon die is wire-bonded to the carrier pads and attached to the lead frame using non-conductive adhesives. Other smaller packaging solutions, as well as alternative bonding techniques such as ball bonding, are either unavailable or unsuitable for the specific dies.

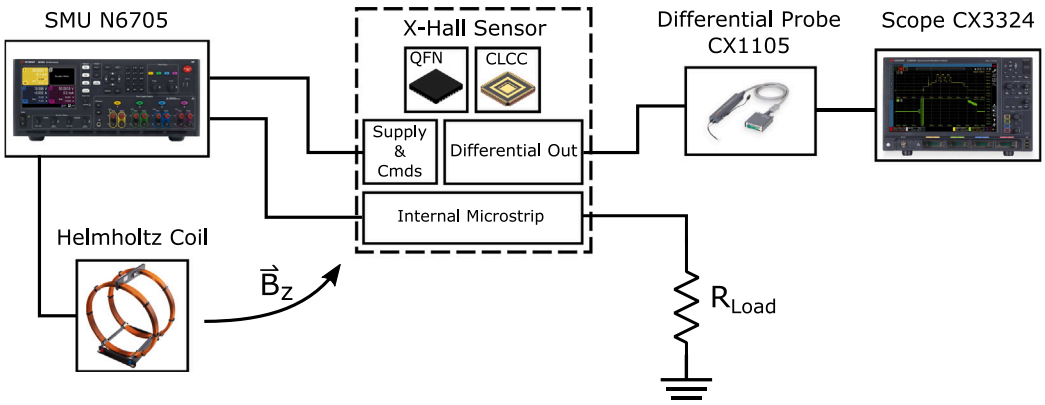


**Fig. 2.** Block diagram of the measurement setup for static, thermal, and noise analysis of the X-Hall sensors under test.

## 3. Static characterization

### 3.1. Measurement setup

The devices-under-test (DUTs) are first characterized statically by using the setup depicted in Fig. 2. The X-Hall sensor samples can be tested by either applying a constant current flowing through the internal microstrip trace or generating a known external static magnetic field, whose lines of force cross the plane of the sensor along the perpendicular direction. In the first case, the source/measurement unit (SMU, Keysight N6780) injects a known static current into the internal chip trace, while no other external excitation is applied.

In the second case, the internal microstrip trace is kept floating, and the SMU is used to inject a known static current $I$ through a Helmholtz coil (3B Scientific 1000906, with a maximum range of −1.5 mT to 1.5 mT), so as to generate a known, constant external $B_z$ field along the longitudinal $z$-axis at the center of the coil, which satisfies the following relationship:

$$B_z = \left(\frac{4}{5}\right)^{\frac{3}{2}} \mu_0 \frac{n}{R} I, \tag{1}$$

where $R = 150$ mm is the radius of the coil, $n = 124$ is the number of windings, and $\mu_0$ is the air magnetic permeability. According to the coil design [21], the variations of $B_z$ and the other field components are negligible at the center of the coil. The differential output voltage $V_{out}$ of the X-Hall sensors is detected using a differential voltage probe (Keysight CX1105) connected to an oscilloscope (Keysight CX3324 waveform analyzer).

These testing methodologies represent two possible application cases. In the first case, which targets low-current applications, the geometrical distance between the measurand current and the X-Hall probe is under control and constant, but the $B_z$ field might result to be neither uniform nor homogeneous on the probe surface [22]. In the second case, targeting high-current applications, e.g., broadband measurement of phase currents in automotive inverters, a well-defined distance is configured between the source of the external magnetic field and the Hall device, so that the magnetic field can be assumed to be homogeneous on the probe surface. However, uncertainties on the actual positioning and vibrations can affect the measurement [22].

### 3.2. Package spread analysis

Each version (CH09 and CH10 shown in Figs. 3 and 4, respectively) was tested using either the CLCC (circle markers) or the QFN (cross markers) package. The tests were conducted under two gain configurations: high gain (blue lines) and low gain (red lines). The high-gain mode is designed to achieve twice the sensitivity of the low-gain mode.

Firstly, the magnetic static response of the sensors was measured by sweeping the external field $B_z$ from −1.5 mT to 1.5 mT (Figs. 3a and 4a). The slope and zero-field intercept, extracted using least-squares regression, represent the magnetic sensitivity $S_B$ (i.e., the current sensitivity $S_A$ of the Hall probe multiplied by the electronic gain of the integrated front end [22]) and the output-referred offset $V_{OS}$, respectively. A corresponding experiment was performed by exciting the sensor with a current flowing through the internal microstrip trace, ranging from −200 mA to 200 mA (Figs. 3b and 4b).

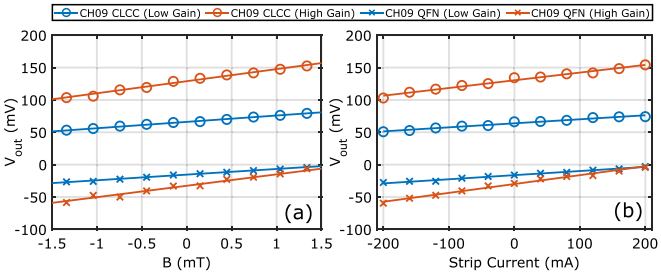


**Fig. 3.** Output voltage $V_{out}$ of the sensor version CH09 (QFN and CLCC packages) while sweeping (a) the external magnetic field $B_z$, and (b) the internal microstrip trace current.

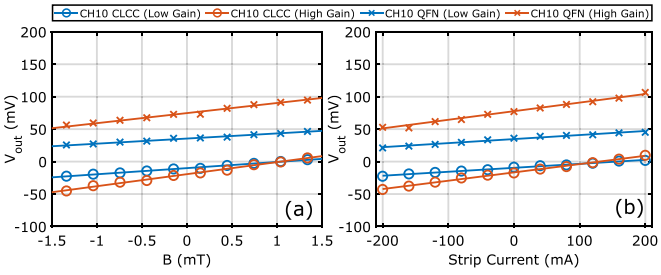


**Fig. 4.** Output voltage $V_{out}$ of the sensor version CH10 (QFN and CLCC packages) while sweeping (a) the external magnetic field $B_z$, and (b) the internal trace current.

A statistical analysis was then performed by considering 20 samples for each sensor configuration. Fig. 5 shows the distribution of the magnetic sensitivity $S_B$ for the four configurations, while the input-referred offset $B_{OS} = \frac{V_{OS}}{S_B}$ is shown in Fig. 6. The mean value of the sensitivity $\hat{S}_B$ and its standard deviation $\sigma(S_B)$ are listed in Table 1, along with the corresponding statistics for $V_{OS}$ and $B_{OS}$.

The tests clearly show that the CLCC package increases the absolute sensitivity by nearly 10% compared to the QFN, with the effect being more pronounced in the CH10 version, which also exhibits reduced process variation due to the optimized design of the feedback resistor

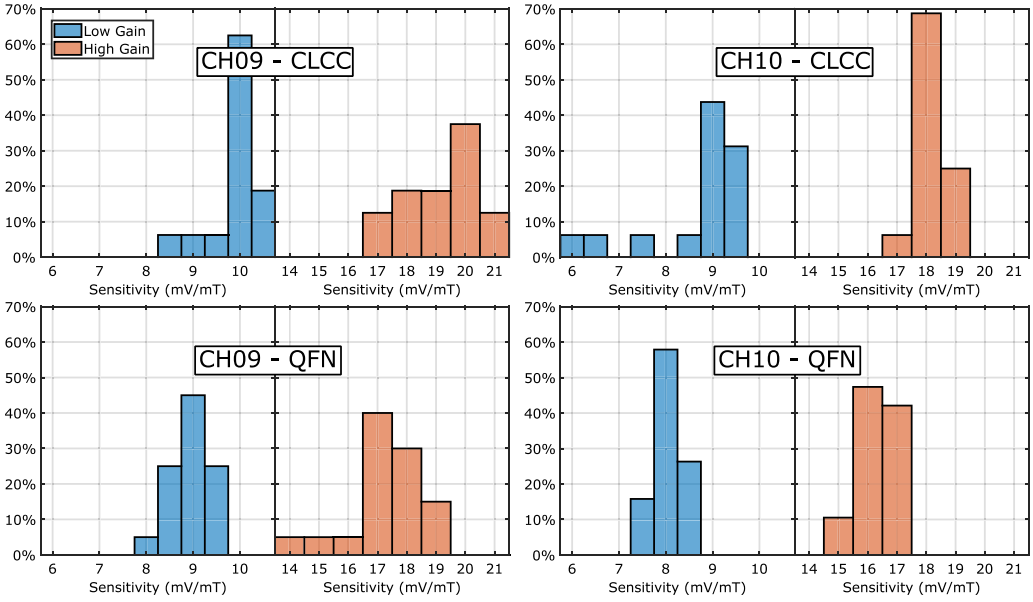


**Fig. 5.** Distribution of the magnetic sensitivity $S_B$ across 20 samples for each configuration.

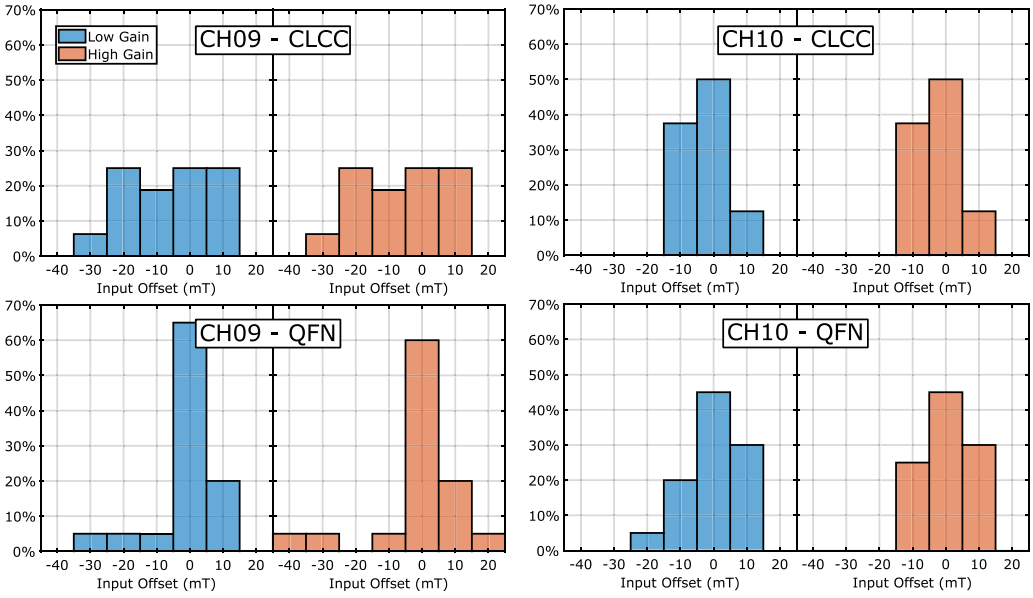


**Fig. 6.** Distribution of the magnetic input-referred offset ($B_{os}$) across 20 samples for each configuration.

in the TIA, realized in this case using a p-doped unsilicided polysilicon technology. The sensitivity increase can be attributed to the metallized areas of the CLCC package (such as the taped lid in this specific case), which are typically electroplated with nickel, a magnetic material. As a result, the external magnetic field becomes slightly more concentrated on the chip.

To further analyze the magnetic effect induced by the CLCC package, the statistical characterization was extended to the case of excitation through the internal microstrip trace (Fig. 7). The results, in terms of the mean current sensitivity $\hat{S}$ and standard deviation $\sigma(S)$ for the four sensor configurations, are listed in Table 2. In this case, there is no clear dependence on the package type, which can be explained by the fact that the current-carrying trace is located close to the magnetic probe, whereas the package is farther away and therefore has negligible magnetic influence.

Notably, for the CH10 samples, the values of the current-to-magnetic field transduction factor ($G_{IB}$) of the internal trace, estimated as the ratio $\hat{G}_{IB} = \frac{\hat{S}}{\hat{S}_B}$ from the data in Tables 1 and 2, are fully consistent with the nominal value of 7.5 mT/A obtained by finite element method (FEM) simulation [16], confirming the negligible magnetic effect of the plastic package. Moreover, the relative standard deviations for the sensitivity values range from 4% to 13%, for both magnetic sensitivity $S_B$ and current sensitivity $S$. This suggests a negligible effect of the variability of the distance between the X-Hall device and the internal microstrip trace. The few outliers in the sensitivity histograms (Figs. 5 and 7) are marginal, but nonetheless highlight the need for improvements in the fabrication process.

The magnetic input-referred offset $B_{OS}$ histograms shown in Fig. 6 exhibit a large technological spread across all sensor configurations. This is a typical characteristic of Hall-effect probes, and the values reported here are consistent with those of X-Hall sensors found in

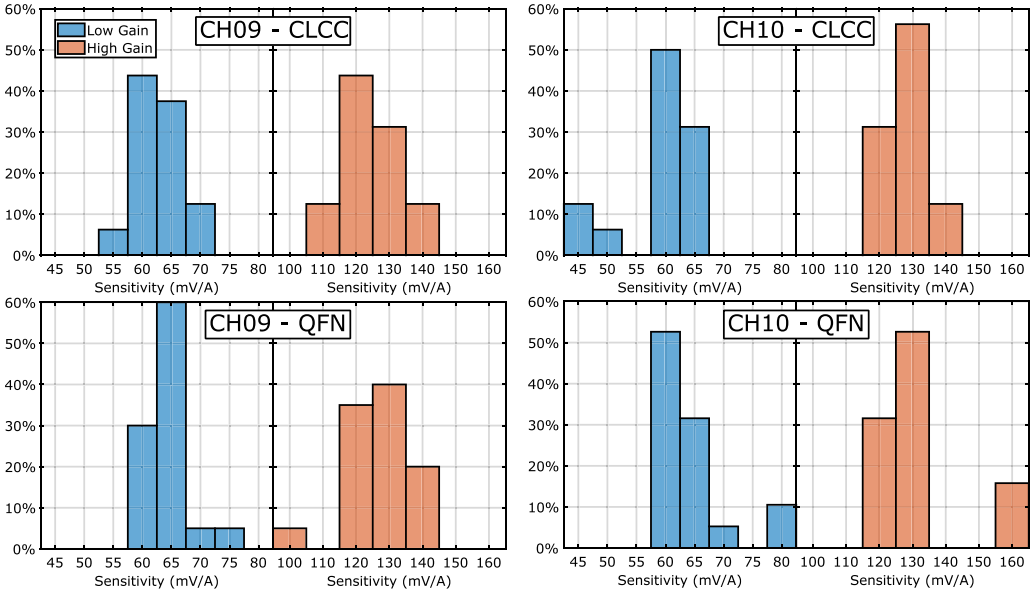


**Fig. 7.** Distribution of the internal microstrip trace current sensitivity $S$ across 20 samples for each configuration.

**Table 1**
Static characteristics of current sensors used as magnetic field detectors. The statistics are extracted on 20 samples for each configuration of sensor version, package, and gain mode.

| Sensor Version | Package | Gain Mode | $\hat{S}_B$ (mV/mT) | $\sigma(S_B)$ (mV/mT) | $\hat{V}_{OS}$ (mV) | $\sigma(V_{OS})$ (mV) | $\hat{B}_{OS}$ (mT) | $\sigma(B_{OS})$ (mT) |
|---|---|---|---|---|---|---|---|---|
| CH09 | CLCC | High | 19.2 | 1.2 | −140 | 230 | −8 | 13 |
| | | Low | 9.89 | 0.50 | −80 | 120 | −8 | 12 |
| | QFN | High | 17.3 | 1.2 | −20 | 180 | −2 | 12 |
| | | Low | 9.04 | 0.44 | −11 | 94 | −1 | 10 |
| CH10 | CLCC | High | 18.10 | 0.63 | −10 | 150 | −2.2 | 6.6 |
| | | Low | 8.5 | 1.1 | −3 | 68 | −2.1 | 6.3 |
| | QFN | High | 16.30 | 0.47 | 10 | 120 | 0.4 | 7.2 |
| | | Low | 8.01 | 0.30 | 3 | 59 | 0.4 | 7.4 |

**Table 2**
Static characteristics of current sensors using the $B_z$ field transduction of the internal metal trace. Statistics are extracted across 20 samples for all the configurations of the sensors.

| Sensor Version | Package | Gain Mode | $\hat{S}$ (mV/A) | $\sigma(S)$ (mV/A) | $\hat{T}$ (mT/A) | $\sigma(T)$ (mT/A) |
|---|---|---|---|---|---|---|
| CH09 | CLCC | High | 124 | 10 | 6.47 | 0.43 |
| | | Low | 62.5 | 4.1 | 6.32 | 0.32 |
| | QFN | High | 127 | 8.7 | 7.33 | 0.34 |
| | | Low | 64.1 | 3.2 | 7.11 | 0.46 |
| CH10 | CLCC | High | 129 | 5.7 | 7.08 | 0.28 |
| | | Low | 58.9 | 7.3 | 6.90 | 0.28 |
| | QFN | High | 135 | 20 | 8.26 | 0.28 |
| | | Low | 63.6 | 5.6 | 7.96 | 0.90 |

the literature [15,16,20]. For example, although the X-Hall device in [15] was fabricated using a different technology node, the standard deviation of $B_{OS}$ (Table 1) aligns with the values reported in this work.

In [20], the X-Hall probe realized using BCD10 technology (with a process iteration similar to that of CH09 in this paper) was characterized directly on-wafer using a probe station and a dedicated measurement setup. Since the values reported in [20] refer to the offset voltage measured directly at the probe output, without any electronic amplification, they cannot be directly compared with those presented in this paper.

For a fair evaluation, the offset values must be compared in terms of the input current $\hat{I}_{OS}$, obtained by dividing $\hat{V}_{OS}$ by the estimated current sensitivity $\hat{S}$, as summarized in Table 3. The optimized matching and improved design of CH10 allowed for achieving a low mean offset, although the overall offset spread (expressed by the standard deviation) is comparable to that of CH09 and considerably higher than the values reported in [20]. The degradation in offset performance can be attributed to the additional contribution of the analog front-end (AFE), as well as mechanical stress from the package, which introduces further offset via the piezo-Hall effect [23]. Due to these effects, evaluating the offset after encapsulation in the final package provides more realistic results for the final application.

**Table 3**
Comparison between the CH09/CH10 packaged samples in high-gain mode against the on-wafer X-Hall probe die fabricated in BCD10 technology reported in [20].

| Sensor | $\hat{S}$ (mV/A) | $\hat{I}_{OS}$ (A) | $\sigma(I_{OS})$ (A) |
|---|---|---|---|
| BCD10 [20] | 0.85 | −0.52 | 0.65 |
| CH09 | 120 | −1.1 | 1.8 |
| CH10 | 130 | 0.1 | 1.1 |

## 4. Dynamic range

To characterize the dynamic range of the sensors, the noise floor and saturation levels were measured using the setup described in Section 3. Referring to Fig. 2, the output noise spectral density $V_{out,\mathrm{noise}}(f)$ is estimated by sampling the differential output voltage at $f_s = 100$ MSa/s, with no input excitation applied to the sensor. Fig. 8 shows the acquired $V_{out,\mathrm{noise}}(f)$ for the CH09 and CH10 versions of the sensor in the low- and high-gain configurations.

The RMS value is obtained by integrating $V_{out,\mathrm{noise}}(f)$ in the designed BW of the sensor:

$$V_{out,noise}^{RMS} = \sqrt{\int_{f_{min}}^{f_{max}} \left|V_{out,\mathrm{noise}}(f)\right|^2 df}, \tag{2}$$

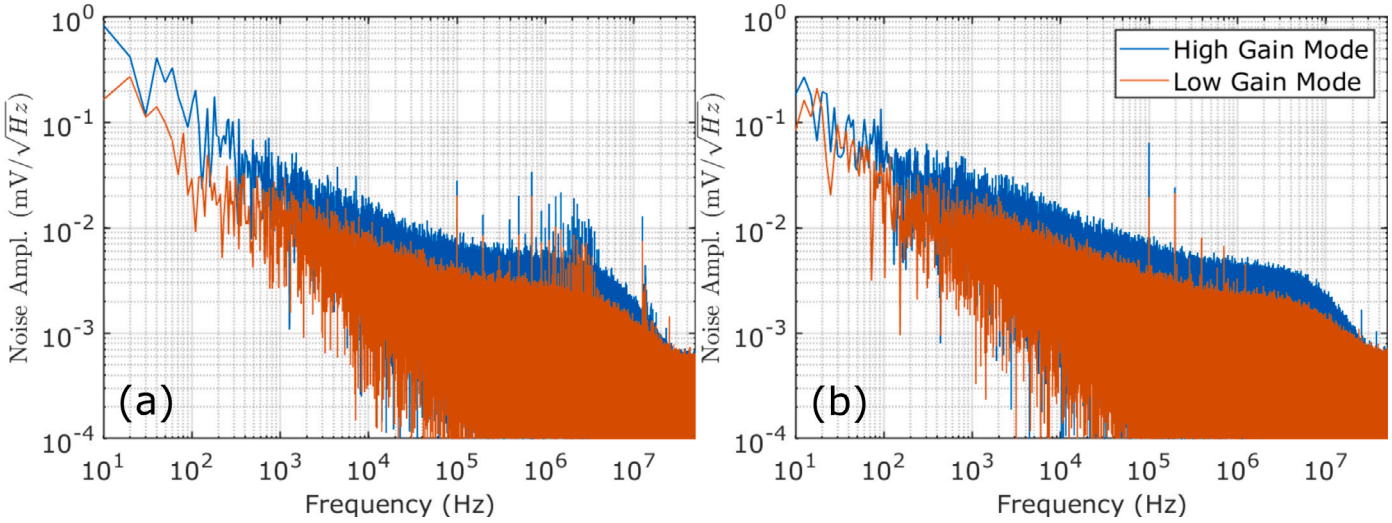


**Fig. 8.** Output noise spectra of the (a) CH09 and (b) CH10 in QFN package in high-gain mode (blue lines) and low-gain mode (red lines).

where $f_{min} = 10$ Hz and $f_{max} = 10$ MHz.

The RMS input-referred noise in terms of the magnetic field ($B_{in,\text{noise}}^{\text{RMS}}$) is obtained by referring $V_{out,\text{noise}}(f)$ to the input using the current sensitivity frequency response $S(f)$ (Section 6), and assuming a constant transduction factor ($T$) of the internal metal trace (Table 2):

$$B_{in,noise}^{RMS} = \sqrt{\int_{f_{min}}^{f_{max}} \left| \frac{V_{out,\text{noise}}(f)}{S_B(f)} \right|^2 df}, \tag{3}$$

where $S_B(f) = S(f)T$ is the magnetic sensitivity of the device.

The linear range is characterized by sweeping the input magnetic field up to device saturation (Fig. 9), i.e., up the maximum and minimum output voltages. The saturation has been defined as the input level required to compress the sensitivity $S_B$ by 1 dB relative to its small-signal value (reported as $\text{Range}_{1\text{-dB}}$ in Table 4). Since the package technology does not affect noise performance, Table 4 summarizes the data collected for CH09 and CH10 in their QFN versions only, showing that the input-referred magnetic noise is almost independent of the AFE gain. As a result, the dynamic range is generally higher for sensors operating in low-gain mode.

The main noise sources for this sensor architecture are the Hall probe itself, the operational amplifier, and the feedback resistor $R_F$ used in the TIA. The noise power contributions referred to the probe–AFE interface can be expressed as:

$$i_{n,\text{tot}}^2 = n_H^2 + i_n^2 + \frac{4kT}{R_F} + e_n^2 \left(1 + \frac{R_F}{R_H}\right)^2 \frac{1}{R_F^2} \approx n_H^2 + i_n^2 + \frac{e_n^2}{R_H^2}, \tag{4}$$

where $n_H$ is the output noise of the Hall device, including both thermal and flicker components [23], $k$ is the Boltzmann constant, $R_H$ is the output resistance of the Hall probe (ranging between 1 kΩ and 4 kΩ [20]), and $e_n$ and $i_n$ are the voltage and current input-referred noise of the operational amplifier, respectively, including both thermal and flicker components. Regardless of the sensor's gain mode, $R_F$ (either 90 kΩ or 200 kΩ) is considerably higher than $R_H$, making the total noise power almost independent of the electronic gain.

Between the two sensor versions, the CH10 was designed with an optimized low-noise operational amplifier, providing an expected noise reduction (based on simulation) of approximately 30% within the 10 MHz BW. Measurements reported in Table 4 show that CH10 demonstrates slightly better noise performance, confirming the influence of this noise source on the overall noise budget, while at the same time indicating that further efforts to reduce AFE noise are not justified given its limited contribution to the overall input-referred noise.

**Table 4**
1-dB range, output and input referred noise, and dynamic range for CH09 and CH10 in QFN package.

| Sensor Version | Gain Mode | $V_{out,noise}^{RMS}$ (mV) | $B_{in,noise}^{RMS}$ (mT) | $\text{Range}_{1\text{-dB}}$ (mT) | Dynamic Range (dB) |
|---|---|---|---|---|---|
| CH09 | High | 3.9 | 0.23 | 63.2 | 48.8 |
| | Low | 2.1 | 0.20 | 126 | 56.0 |
| CH10 | High | 3.2 | 0.17 | 100 | 55.4 |
| | Low | 1.7 | 0.17 | 172 | 60.1 |

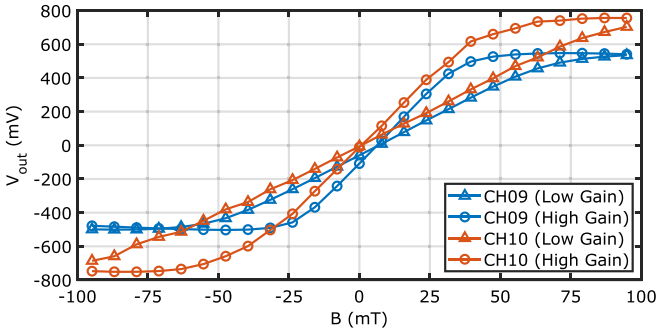


**Fig. 9.** $V_{out}$ saturation of the sensor version CH09 and CH10 in QFN package. Each version is tested in the two gain configurations (high- and low-gain modes).

## 5. Thermal characterization

Since the X-Hall topology does not rely on the dynamic offset cancellation provided by the spinning current technique, the temperature dependence of the transduction gain and offset is one of the most critical metrics to evaluate. Indeed, even a small temperature drift can result in a deviation of the estimated magnetic field by up to a few mT.

This issue becomes even more critical considering that the temperature can vary by more than 100 °C in typical power electronics applications. For this reason, a static characterization using a climatic chamber (ACS DY110) was repeated for one sample of each sensor configuration by performing a temperature sweep from −20 °C to 80 °C in 5 °C steps. At each temperature setpoint, a complete static characterization was carried out in the presence of a homogeneous

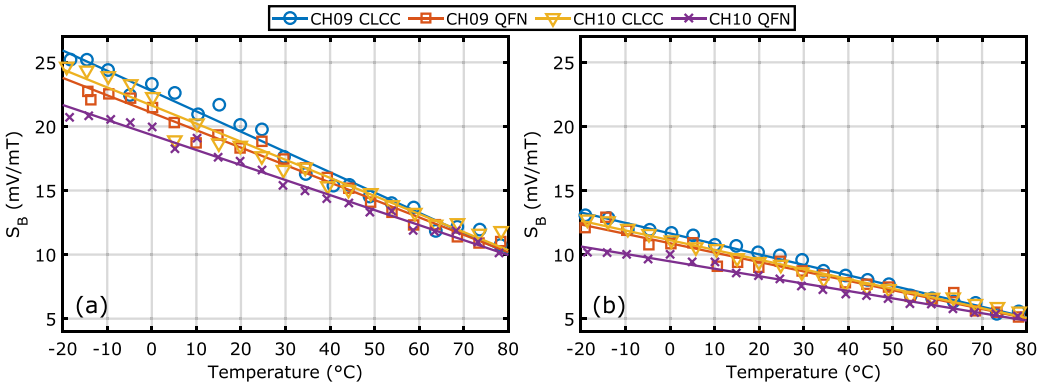


**Fig. 10.** Static characterization of one sample for each current sensor version. Absolute value of the magnetic sensitivity $S_B$ for the (a) high-gain and (b) low-gain modes over a 100°-C temperature range.

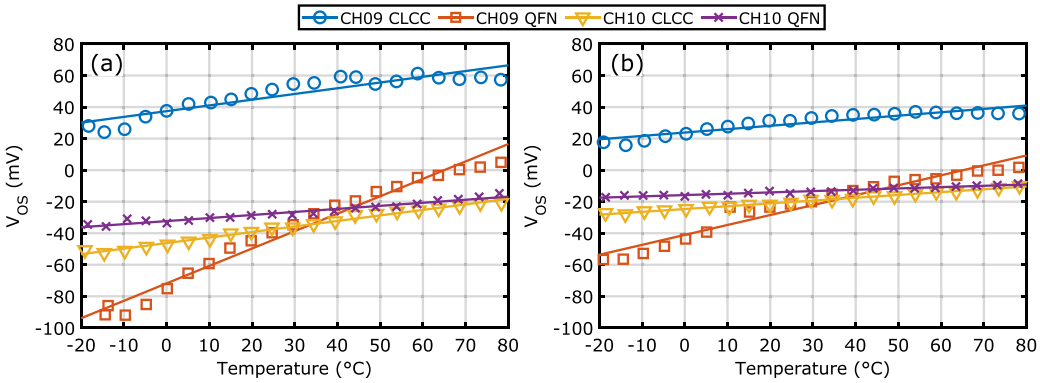


**Fig. 11.** Absolute values of the output-referred offset $V_{OS}$ for the (a) high-gain and (b) low-gain modes over a 100 °C temperature range.

magnetic field generated by the Helmholtz coil, with the DUT operating in both high- and low-gain modes.

Fig. 10 shows the temperature dependence of the absolute value of $S_B$, where the temperature coefficient is obtained by linear regression. Based on the data in Table 5, the temperature dependence of magnetic sensitivity is similar across all configurations, with a minor improvement in CH10 compared to CH09 due to the better temperature performance of the feedback resistors. In any case, the X-Hall probe, like any Hall device, exhibits a noticeable temperature dependence that requires an active compensation circuit to achieve industrially acceptable dispersion levels, as demonstrated in [14].

A similar thermal analysis was performed for the output-referred offset $V_{OS}$, with results shown in Fig. 11. The slope values in Table 6 indicate a smaller offset variation in low-gain mode compared to high-gain mode for both package technologies. However, based on the data obtained for the input-referred offset (see Fig. 12 and Table 7), there is no significant difference between the high-gain and low-gain modes, indicating that the differences observed in the output-referred offset are mainly due to the different sensitivity levels in the two operating modes. Finally, the temperature dependence of the offset observed in the CH10 version is considerably lower than that of CH09. Also this improvement can be attributed to the optimized design of the AFE in CH10.

**Table 5**
Absolute and relative slopes of the dependence of magnetic sensitivity on temperature for all tested current sensor versions (Fig. 10).

| Sensor Version | Package | Gain Mode | Absolute Slope ($\frac{mV}{mTK}$) | Relative Slope ($\frac{\%}{K}$) |
|---|---|---|---|---|
| CH09 | CLCC | High | −0.16 | −0.80 |
| | | Low | −0.082 | −0.80 |
| | QFN | High | −0.14 | −0.77 |
| | | Low | −0.071 | −0.79 |
| CH10 | CLCC | High | −0.14 | −0.76 |
| | | Low | −0.075 | −0.80 |
| | QFN | High | −0.12 | −0.69 |
| | | Low | −0.058 | −0.67 |

**Table 6**
Absolute and relative slopes of the dependence of the output-referred offset on temperature for all tested current sensor versions (Fig. 11).

| Sensor Version | Package | Gain Mode | Absolute Slope ($\frac{mV}{K}$) | Relative Slope ($\frac{\%}{K}$) |
|---|---|---|---|---|
| CH09 | CLCC | High | −0.36 | −0.74 |
| | | Low | −0.21 | −0.69 |
| | QFN | High | −1.1 | −2.5 |
| | | Low | −0.63 | −3.1 |
| CH10 | CLCC | High | −0.35 | −0.89 |
| | | Low | −0.18 | −0.96 |
| | QFN | High | −0.19 | −0.67 |
| | | Low | −0.084 | −0.61 |

## 6. Dynamic characterization

### 6.1. Measurement setup

The frequency response of the X-Hall devices employed as current sensors has been tested with the setup depicted in Fig. 13. Three different dynamic conditions were considered:

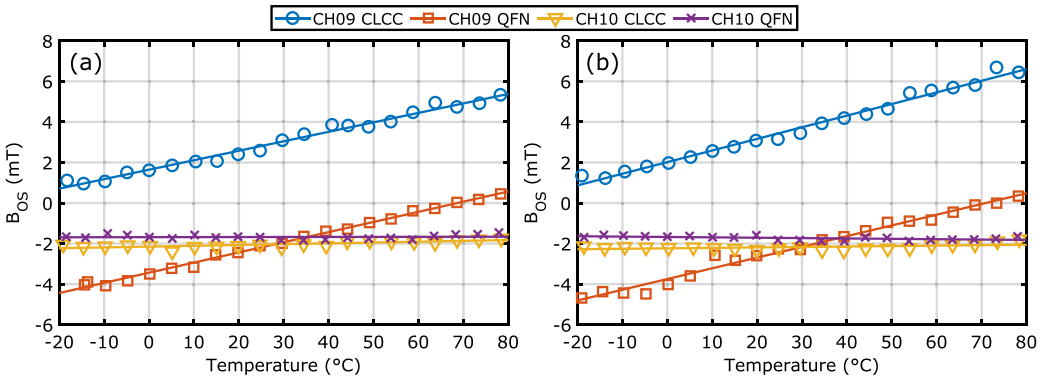


**Fig. 12.** Absolute values of the input-referred offset $B_{OS}$ for the (a) high-gain and (b) low-gain modes over a 100 °C temperature range.

**Table 7**
Absolute and relative slopes of the dependence of the input-referred offset on temperature for all tested current sensor versions (Fig. 12). The relative dependence is calculated on the nominal offset (at 20 °C).

| Sensor Version | Package | Gain Mode | Absolute Slope ($\frac{\mu T}{K}$) | Relative Slope ($\frac{\%}{K}$) |
|---|---|---|---|---|
| CH09 | CLCC | High | −47 | −1.8 |
| | | Low | −57 | −1.8 |
| | QFN | High | −50 | −2.0 |
| | | Low | −53 | −2.0 |
| CH10 | CLCC | High | −2.3 | −0.10 |
| | | Low | −4.0 | −0.19 |
| | QFN | High | 0.28 | 0.016 |
| | | Low | 1.8 | 0.11 |

1. *Small-signal single-frequency sweep*. A sinusoidal current excitation $I_{in}^{RMS}$ = 40 mA provided by an arbitrary waveform generator (AWG, Siglent SDG2122) is applied to the integrated microstrip of the sensor at frequencies up to 10 MHz. The current flows into a 5-$\Omega$ load resistor through a reference current probe (Tektronix TCPA300). Both $v_{out}$ and the input current $i_{in}$ are measured by an oscilloscope (Keysight CX3324 waveform analyzer), exploiting coherent averaging to decrease the noise floor. In this case, the SMU is turned off.
2. *Large-signal magnetic field step*. A current step (of up to 10 A) is applied through an external busbar to the load using an SMU (Keysight B2900). As shown in Fig. 13b, the magnetic field generated by the current flowing into the external wire is detected by the sensor.
3. *Large-signal current step*. A current step (of up to 0.3 A) is applied to the internal microstrip. The acquisition is the same as for the CW test, while the step is applied by the SMU.

### 6.2. Dynamic data analysis

The small-signal frequency response of the current sensitivity $S$ is shown in Fig. 14 and clearly reveals the presence of an inductive parasitic effect across all the considered versions. According to [15], this effect can be modeled as an additive perturbation, such that the measured output voltage of the Hall sensor can be expressed as

$$V_{\text{out}}(f) = S(f)I_{\text{in}}(f) + \Delta V_{\text{out}}(f) \approx$$
$$\approx S I_{\text{in}}(f) + 2\pi f I_{\text{in}}(f) L_{\text{stray}} = \left(S(f) + 2\pi f L_{\text{stray}}\right) I_{\text{in}}(f), \quad (5)$$

where $I_{\text{in}}$ is the current flowing through the internal microstrip trace, and $L_{\text{stray}}$ is the parasitic inductance that couples $I_{\text{in}}$ with the sensor output voltage $V_{\text{out}}$.

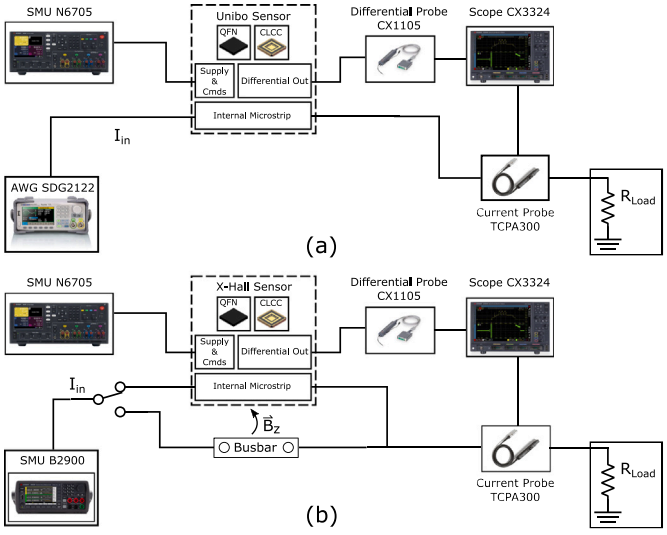


**Fig. 13.** Block diagram of the setup for the (a) CW small signal and (a) large signal dynamic characterization of the X-Hall sensors.

The measured sensitivity values $\hat{S}$ at high test frequencies are consistent with the presence of a parasitic inductance as low as a few nH. This inductance can be partially explained by parasitic coupling between bond wires. Indeed, although the sensitive output wires were kept distant from those used to carry the input current, typical arc models for bond wires (neglecting the effect of the lead frame) estimate an inductive contribution of up to 1 nH. The few nH observed experimentally appear to be a reasonable overall value when considering electromagnetic interference (EMI) from the silicon, package, and setup levels.

Since the layout is nearly identical for both CH09 and CH10, with the same dimensions and distances between the current-carrying trace and the output lines, it is not possible to extract quantitative information about inductive coupling at the silicon level. Regarding the package, the use of either a small plastic or larger ceramic package (with longer bond wires) appears to have a negligible effect on the dynamic parasitic behavior, as clearly shown in Fig. 14b. However, these results confirm that EMI-induced limitations on the dynamic response of broadband current sensors remain a critical challenge in the design of magnetic-probe-based solutions, whether using Hall-effect sensors [24] or magnetoresistive sensors [25].

Measuring the step response is a standard methodology for validating current sensors in power electronics. However, generating large current steps with high time derivatives is a challenging task from an instrumentation perspective, as it is limited by both the setup configuration and the capabilities of the available equipment. Hence, it is worth

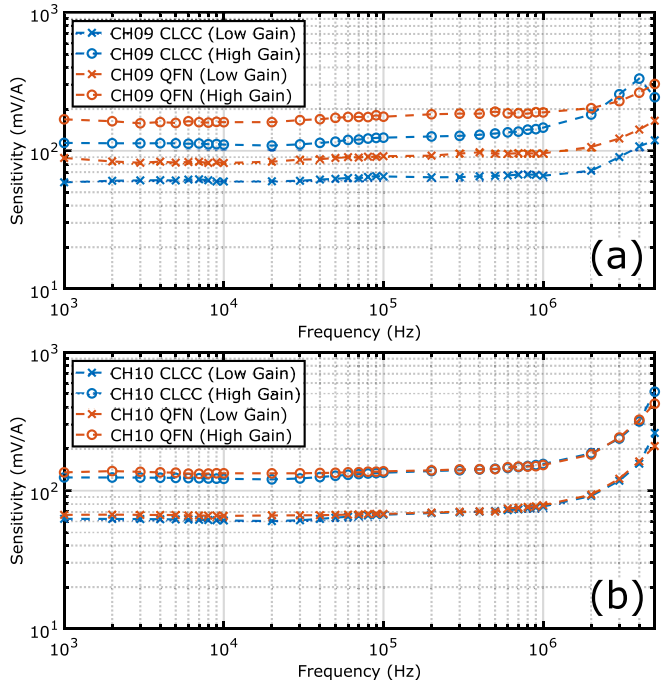


**Fig. 14.** Magnitude of the frequency response of the (a) CH09 and (b) CH10 version of the X-Hall sensor.

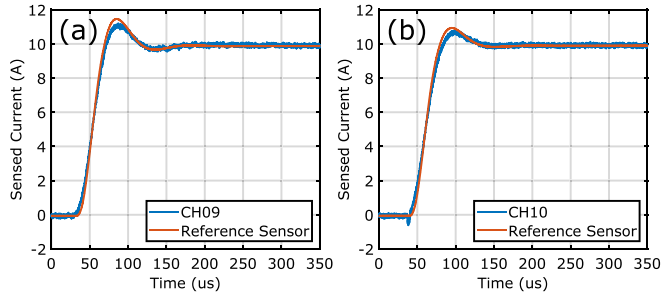


**Fig. 15.** (a) CH09 and (b) CH10 response to a single step current excitation applied to the external busbar (QFN package).

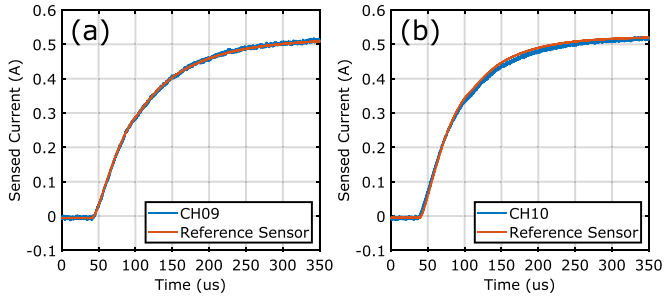


**Fig. 16.** (a) CH09 and (b) CH10 response to a single step current excitation applied to the internal trace (QFN package).

noting that this approach is not the most suitable for investigating the wideband behavior of sensors.

Nevertheless, the available DUTs were here tested also in terms of their large-current step response using the setup configuration described in the previous subsection. Fig. 15 shows the response of CH09 and CH10 in the QFN package when an external stepped magnetic field $B_z$ is applied, as generated by the excitation current sourced by the

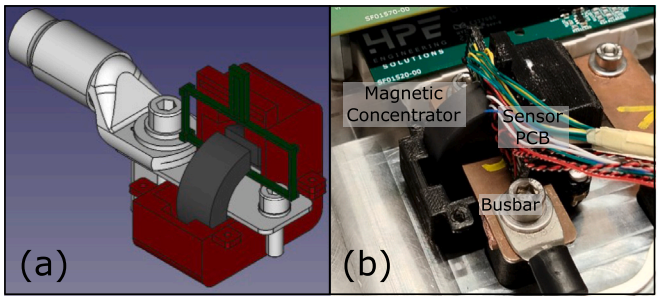


**Fig. 17.** (a) Rendering of the tested prototype with the magnetic concentrator (black), the plastic fixture (red) and the circuit broadband holder (green). (b) Picture of the CH10-QFN Hall sensor prototype including the magnetic concentrator placed on the target busbar.

SMU and delivered to a suitable load through an external busbar capable of handling high current levels. The output voltage in both high- and low-gain modes (blue lines) closely follows the reference excited current (red lines). Notably, in this configuration, the excitation current exhibits the typical response of a second-order system, described by the following current-to-current transfer function:

$$H_{busbar}(s) = \frac{1}{\frac{1}{\omega_n^2}s^2 + \frac{\delta}{\omega_n}s + 1}, \tag{6}$$

with a natural frequency $\omega_n = 74000$ rad/s and a damping ratio $\delta = 0.50$, limiting the frequency of the excitation to about 12 kHz.

Conversely, when the large-signal step is applied directly through the internal trace (Fig. 16), the current response aligns with that of a first-order system, described by the following transfer function:

$$H_{\text{internal}}(s) = \frac{1}{\frac{\tau}{2\pi}s + 1}, \tag{7}$$

which is consistent with the dominant inductive behavior of the internal S-shaped trace used to enhance magnetic coupling with the probe. The model fitted to the step response yields a time constant of $\tau_{CH09} = 67.0$ µs for CH09 and $\tau_{CH10} = 51.9$ µs for CH10, corresponding to an excited BW of less than 3 kHz.

## 7. Application to SiC traction inverter

The evaluation presented in the previous sections highlighted that the CH10 version in the QFN package, operating in low-gain mode, outperforms the other configurations in terms of both dynamic range and temperature resilience. Therefore, this version was selected to test the sensor in the application case, namely measuring the current flowing through one phase of a SiC traction inverter.

To successfully integrate this sensor and adapt its native magnetic range to the high currents expected in an inverter, a ferromagnetic core concentrator was designed and manufactured. This concentrator addresses both the mechanical fit with the inverter busbar and the need to handle a target current range of ±300 A. The TDK K1 (a NiZn alloy) was selected as the material for the concentrator due to its linear magnetization across the operating range and its constant relative magnetic permeability up to 10 MHz, thus preserving the broadband capability of the sensor. A rendering of the Hall sensor integrated with the magnetic concentrator is shown in Fig. 17a.

Using a measurement setup analogous to that shown in Fig. 13b, the sensitivity of the sensor prototype was first determined by sweeping a static current through the busbar (Fig. 18a), resulting in a sensitivity of $S = 2.0$ mV/A in low-gain mode and $S = 4.2$ mV/A in high-gain mode. These values are consistent with the transduction factor $\frac{B_{\text{gap}}}{I_{\text{bar}}} \simeq 0.24$ mT/A of the magnetic concentrator and are well aligned with the design expectations. Therefore, the range and noise level of

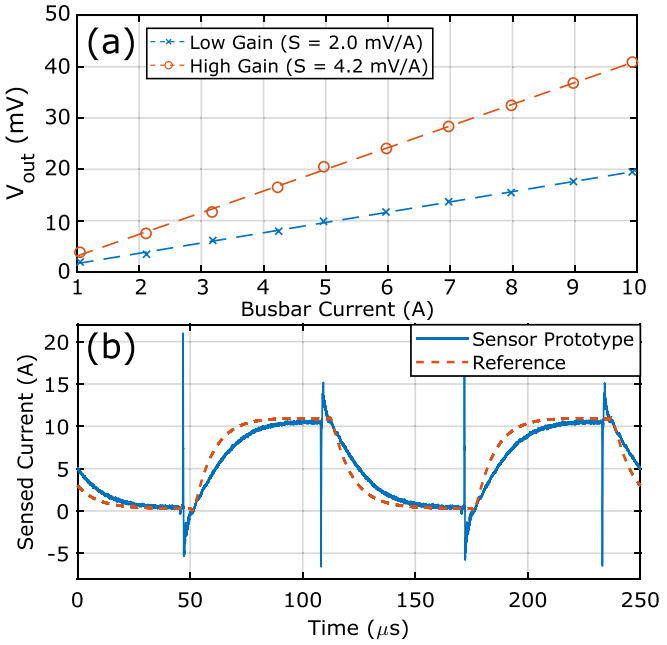


**Fig. 18.** (a) Sensitivity of the sensor prototype including the magnetic interface, and (b) measurement of the stepped current generated by the inverter on the busbar.

Table 4 can be adapted using the transduction factor of the magnetic concentrator.

The final values are reported in Table 8, along with a comparison of the prototype main characteristics with those of three commercial sensors. It should be noted, however, that commercially available purely-Hall devices with MHz-range capabilities perform current sensing through an internal metal trace integrated into the package, which limits their maximum measurable range. Conversely, wideband and high-current sensors typically rely on hybrid solutions (i.e., Hall combined with Rogowski). Although this makes the comparison not entirely fair, it remains relevant for positioning the proposed purely Hall prototype among other commercially available solutions.

The demonstrator SiC traction inverter by HPE used for testing is based on an ADP480120W3 SiC power module and is rated for a 800 V voltage class and a 250 kW power class. Preliminary measurements and validation were conducted by positioning the integrated sensor prototype including the concentrator on one of the output busbars inside the inverter housing (Fig. 17b). During these tests, the sensor prototype was set up to detect the current flowing through a resistive load, with the inverter phase controlled to switch from 0 V to 64 V at an 8 kHz frequency and 50% duty cycle.

The experimental results, shown in Fig. 18b, demonstrate that the prototype response is fairly aligned with that of a commercial sensor used as a reference (PEM CWT6 Rogowski coil with a 3-dB-BW of 16 MHz). However, output voltage spikes are observed during switching events. This behavior was not encountered during laboratory tests under similar operating conditions, suggesting that the spikes may be attributed to capacitive coupling between the high-voltage busbar and the sensor output in the actual inverter environment. This highlights that, while the sensor and its magnetic interface perform as expected, improved electromagnetic conditions and careful positioning are crucial for mitigating spurious effects in real-world applications.

## 8. Conclusion

This work experimentally analyzed X-Hall current sensors across two versions and two different packages, highlighting several performance-limiting aspects that could arise in the system-level deployment of these devices. The evaluation of different packages and components revealed that the plastic QFN package offered a distinct advantage over the CLCC package due to reduced magnetic effects, lower inductive coupling, smaller size, and overall superior performance.

Static and noise measurements revealed that a low-noise AFE (such as the one in the CH10 version) does not provide significant advantages, as the input-referred noise is primarily dominated by the noise generated by the Hall probe. However, the improvements of the CH10 version in terms of offset stability and dynamic range make it the preferred choice for the final application. Furthermore, it offers the potential for additional performance enhancements by enabling the use of higher bias currents or the second integrated measurement channel.

While inductive parasitic coupling is present at the silicon, package, and test board levels, the output of the tested devices remained fully aligned with the reference current generated by the available measurement setup under both small- and large-current conditions. In conclusion, the CH10 version in the QFN package, operating in low-gain mode, proved to be the best configuration in terms of both dynamic range and temperature resilience.

This sensor candidate was also tested in a preliminary setup within an 800 V SiC traction inverter, and its performance was compared with that of commercial solutions. This use case demonstrates how a specialized sensor like the X-Hall can be tailored and integrated into a complex system to monitor critical electrical currents. This high-performance current sensor requires a precisely designed magnetic interface and a carefully controlled electromagnetic environment to ensure accurate and stable readings under the demanding conditions of an automotive power system.

**Table 8**
Comparison among the proposed prototype and three commercial devices with similar characteristics.

| Sensor Name | 3-dB BW (MHz) | Sensitivity (mV/A) | Range (A) | Input Noise Level (A) |
|---|---|---|---|---|
| This work (CH10 QFN) (High/Low Gain) | 3/3 | 4.2/2.0 | ±200/±350 | 0.71/0.71 |
| Allegro ACS37032 | 5 | 20.3 | ±65[d] | 0.050[a] |
| Melexis MLX91220 | 0.3 | 26.7 | ±75[d] | 0.116[b] |
| LEM FRS 1000-S | 1 | 0.67 | ±3000 | 2.5[c] |

[a] RMS value with 5-MHz integration BW.
[b] RMS value with 300-kHz integration BW.
[c] Peak to peak value with 1-MHz integration BW.
[d] Range of the internal metal trace.

## CRediT authorship contribution statement

**Mattia Mengozzi:** Writing – review & editing, Writing – original draft, Methodology, Investigation, Formal analysis, Data curation. **Sana Fatima Syeda:** Resources. **Jacopo Ferretti:** Investigation. **Gian Piero Gibiino:** Writing – review & editing, Writing – original draft, Supervision, Methodology, Conceptualization, Formal analysis. **Marco Crescentini:** Writing – review & editing, Writing – original draft, Supervision, Methodology, Funding acquisition, Conceptualization. **Pier Andrea Traverso:** Writing – review & editing, Supervision, Conceptualization.

## Declaration of competing interest

The authors declare that they have no known competing financial interests or personal relationships that could have appeared to influence the work reported in this paper.

## Acknowledgments

This work is supported by the R-PODID project, which is funded by the Chips Joint Undertaking and its members, including the top-up funding by the National Authorities of Italy, Turkey, Portugal, The Netherlands, Czech Republic, Latvia, Greece, and Romania under grant agreement No. 101112338.

## Data availability

Data will be made available on request.

## References

[1] Z. Xin, H. Li, Q. Liu, P.C. Loh, A review of megahertz current sensors for megahertz power converters, IEEE Trans. Power Electron. 37 (6) (2021) 6720–6738.

[2] M. Riera-Guasp, J.A. Antonino-Daviu, G.-A. Capolino, Advances in electrical machine, power electronic, and drive condition monitoring and fault detection: State of the art, IEEE Trans. Ind. Electron. 62 (3) (2015) 1746–1759, http://dx.doi.org/10.1109/TIE.2014.2375853.

[3] W. Lang, Y. Hu, C. Gong, X. Zhang, H. Xu, J. Deng, Artificial intelligence-based technique for fault detection and diagnosis of ev motors: A review, IEEE Trans. Transp. Electrification 8 (1) (2022) 384–406, http://dx.doi.org/10.1109/TTE.2021.3110318.

[4] S. Zhao, F. Blaabjerg, H. Wang, An overview of artificial intelligence applications for power electronics, IEEE Trans. Power Electron. 36 (4) (2021) 4633–4658, http://dx.doi.org/10.1109/TPEL.2020.3024914.

[5] A. Patel, M. Ferdowsi, Current sensing for automotive electronics—a survey, IEEE Trans. Veh. Technol. 58 (8) (2009) 4108–4119, http://dx.doi.org/10.1109/TVT.2009.2022081.

[6] H. Yan, Y. Xu, J. Zou, Y. Fang, F. Cai, A novel open-circuit fault diagnosis method for voltage source inverters with a single current sensor, IEEE Trans. Power Electron. 33 (10) (2018) 8775–8786, http://dx.doi.org/10.1109/TPEL.2017.2776939.

[7] Y. Yu, Y. Zhao, B. Wang, X. Huang, D. Xu, Current sensor fault diagnosis and tolerant control for vsi-based induction motor drives, IEEE Trans. Power Electron. 33 (5) (2018) 4238–4248, http://dx.doi.org/10.1109/TPEL.2017.2713482.

[8] C. Wu, C. Guo, Z. Xie, F. Ni, H. Liu, A signal-based fault detection and tolerance control method of current sensor for pmsm drive, IEEE Trans. Ind. Electron. 65 (12) (2018) 9646–9657, http://dx.doi.org/10.1109/TIE.2018.2813991.

[9] A. Giantomassi, F. Ferracuti, S. Iarlori, G. Ippoliti, S. Longhi, Electric motor fault detection and diagnosis by kernel density estimation and kullback–leibler divergence based on stator current measurements, IEEE Trans. Ind. Electron. 62 (3) (2015) 1770–1780, http://dx.doi.org/10.1109/TIE.2014.2370936.

[10] H. Wang, X. Hu, Q. Liu, G. Zhao, D. Luo, An on-chip high-speed current sensor applied in the current-mode dc–dc converter, IEEE Trans. Power Electron. 29 (9) (2014) 4479–4484.

[11] S. Ziegler, R.C. Woodward, H.H.-C. Iu, L.J. Borle, Current sensing techniques: A review, IEEE Sensors J. 9 (4) (2009) 354–376, http://dx.doi.org/10.1109/JSEN.2009.2013914.

[12] Allegro Microsystems ACS37032 - DC to 5 MHz Current Sensor With Reference or Fault Output.

[13] T. Funk, B. Wicht, A fully integrated DC to 75 MHz current sensing circuit with on-chip rogowski coil, in: Proc. IEEE Custom Integrated Circuits Conference, CICC, IEEE, San Diego, 2018, pp. 1–4.

[14] A. Jouyaeian, Q. Fan, M. Motz, U. Ausserlechner, K.A.A. Makinwa, A 25A hybrid magnetic current sensor with 64 mA resolution, 1.8MHz bandwidth, and a gain drift compensation scheme, in: 2021 IEEE International Solid- State Circuits Conference (ISSCC), vol. 64, IEEE, 2021, pp. 82–84.

[15] M. Crescentini, et al., The x-hall sensor: Toward integrated broadband current sensing, IEEE Trans. Instrum. Meas. 70 (2021) 1–12, http://dx.doi.org/10.1109/TIM.2020.3036764.

[16] S.F. Syeda, M. Crescentini, M. Marchesi, P.A. Traverso, A. Romani, A wideband and low-noise cmos-integrated x-hall current sensor operating in current mode, IEEE Trans. Instrum. Meas. 72 (2023) 1–11, http://dx.doi.org/10.1109/TIM.2023.3284055.

[17] M. Crescentini, M. Marchesi, A. Romani, M. Tartagni, P.A. Traverso, A. broadband, On-chip sensor based on hall effect for current measurements in smart power circuits, IEEE Trans. Instrum. Meas. 67 (6) (2018) 1470–1485, http://dx.doi.org/10.1109/TIM.2018.2795248.

[18] M. Crescentini, M. Biondi, M. Marchesi, A. Romani, M. Tartagni, P.A. Traverso, Bandwidth enhancement in hall probe by x-hall DC biasing, J. Phys.: Conf. Ser. 1065 (2018) 052031.

[19] L. Zhou, J. Li, L. Li, Y. Liu, Y. Xu, A high-sensitivity and low-offset cross-like x-hall device suitable for broadband magnetic sensors fabricated in 180-nm bcd technology, IEEE Trans. Electron Devices 71 (9) (2024) 5652–5659, http://dx.doi.org/10.1109/TED.2024.3423831.

[20] G.P. Gibiino, et al., Experimental evaluation of hall-effect current sensors in bcd10 technology, Measurement 220 (2023) 113289.

[21] E. Bronaugh, Helmholtz coils for calibration of probes and sensors: limits of magnetic field accuracy and uniformity, in: Proceedings of International Symposium on Electromagnetic Compatibility, 1995, pp. 72–76, http://dx.doi.org/10.1109/ISEMC.1995.523521.

[22] M. Crescentini, S.F. Syeda, G.P. Gibiino, Hall-effect current sensors: Principles of operation and implementation techniques, IEEE Sensors J. 22 (11) (2022) 10137–10151.

[23] R. Popovic, Hall Effect Devices, CRC Press, U.S.A, 2003.

[24] O. Aiello, Hall-effect current sensors susceptibility to EMI: experimental study, Electronics (Switzerland) 8 (11) http://dx.doi.org/10.3390/electronics8111310.

[25] H. Zhang, S. Wu, Y. Ouyang, H. Ma, R. Bi, X. Liu, S. Pan, K. Zhou, Q. Jin, B. Lu, J. Hu, A 20-mhz wideband current sensor utilizing a frequency band optimized tunnel magnetoresistance bridge chip, IEEE Sensors J. 25 (5) (2025) 8155–8164, http://dx.doi.org/10.1109/JSEN.2025.3527496.